Journal of Nonlinear Science (2020) 30:3235–3263
https://doi.org/10.1007/s00332-020-09649-2

Anomalous Waves Triggered by Abrupt Depth Changes: Laboratory Experiments and Truncated KdV Statistical Mechanics

Nicholas J. Moore[1] · **C. Tyler Bolles**[2] · **Andrew J. Majda**[3] · **Di Qi**[3]

Received: 3 December 2019 / Accepted: 13 August 2020 / Published online: 3 September 2020

Abstract

Recent laboratory experiments of Bolles et al. (Phys Rev Fluids 4(1):011801, 2019) demonstrate that an abrupt change in bottom topography can trigger anomalous statistics in randomized surface waves. Motivated by these observations, Majda et al. (Proc Natl Acad Sci 116(10):3982–3987, 2019) developed a theoretical framework, based on deterministic and statistical analysis of the truncated Korteweg-de Vries (TKdV) system that successfully captures key qualitative features of the experiments including the robust emergence of anomalous statistics and heightened skewness in the outgoing wavefield. Here, we extend these parallel experimental and modeling efforts with several new findings that have resulted from a synergetic interaction between the two. By precisely relating model parameters to physical ones, we calibrate the model inverse temperature to the specific conditions present in the experiments, thereby permitting a quantitative comparison. We find theoretically predicted distributions of surface displacement to match the experimental measurements with surprising detail. Prompted by the presence of surface slope in the TKdV Hamiltonian, we present new experimental measurements on surface slope statistics and compare them to model predictions. Analysis of some deterministic trajectories of TKdV elucidates the experimental length and time scales required for the statistical transition to a skewed state. Finally, the theory predicts a peculiar relationship between the outgoing displacement skewness and the change in slope variance, specifically how their ratio depends on the wave amplitude and depth ratio. New experimental measurements provide convincing evidence for this prediction.

Communicated by Leslie Smith.

✉ Nicholas J. Moore
nickmoore83@gmail.com

[1] United States Naval Academy, Annapolis, MD, USA

[2] University of Michigan, Ann Arbor, MI, USA

[3] Courant Institute of Mathematical Sciences, New York, NY, USA

1 Introduction

Rogue waves are abnormally large surface waves, defined by oceanographers as those that exceed twice the significant wave height (Müller et al. 2005; Ying et al. 2011). Though such waves were once dismissed as myth, they have now been recorded in oceans across the globe and pose a recognized threat to seagoing vessels and naval structures. Rogue waves, also variously known as freak or anomalous waves, have been observed in shallow (Pelinovsky et al. 2000; Gramstad et al. 2013), intermediate (Karmpadakis et al. 2019), and deep water (Dematteis et al. 2018, 2019), and certain features of rogue waves have been recovered by exact solutions to various wave models (Peregrine 1983; Clarkson and Dowie 2017; Chen and Pelinovsky 2019). These abnormal waves can be triggered by a variety of mechanisms, including anomalous wind-forcing (Kharif et al. 2008; Toffoli et al. 2017), opposing currents (Garrett and Gemmrich 2009; Onorato et al. 2011), focusing due to variable bathymetry (Heller et al. 2008; White and Fornberg 1998), and the Benjamin-Feir deep-water modulational instability (Benjamin and Feir 1967; Viotti et al. 2013; Cousins and Sapsis 2015; Farazmand and Sapsis 2017). The common tie between these mechanisms is their ability to generate non-normal statistics in the surface displacement: when governed by Gaussian statistics, the likelihood of a rogue wave is extremely low, but these events occur much more frequently when surface statistics deviate from Gaussian. In this way, anomalous waves can be approached from the broader perspective of turbulent dynamical systems (Sapsis and Majda 2013a, b, c; Chen and Majda 2016; Majda 2016; Macêdo et al. 2017; Majda and Qi 2018; Blonigan et al. 2019; Guth and Sapsis 2019; Holm 2019).

A recent series of laboratory (Bolles et al. 2019; Trulsen et al. 2020) and numerical investigations (Viotti and Dias 2014; Herterich and Dias 2019) have demonstrated the emergence of anomalous wave statistics from abrupt variations in bottom topography. Since topographical variations are strictly one-dimensional, these studies can be viewed as offering a bare minimum set of conditions capable of generating anomalous waves. In particular, the more complex mechanism of focusing by 2D bottom topography is absent. The studies thus offer a paradigm system, with emergent anomalous features similar to those seen in more complex systems, but in a tractable context that is amenable to analysis.

Our particular focus is the laboratory experiments of Bolles et al. (2019), who demonstrated the emergence of anomalous statistics from a randomized wavefield encountering an abrupt depth change (ADC). In these experiments, the incoming wavefield is generated with nearly Gaussian statistics, and a plexiglass step placed near the middle of the tank creates the depth change. Upon passing over the step, the wave distribution skews strongly toward positive displacement, with deviation from Gaussian being most pronounced a short distance downstream of the ADC. Inspired by these experimental observations, Majda et al. (2019)) developed a theoretical framework that accurately captures several key aspects of the anomalous behavior. The theory is based on deterministic and statistical analysis of the truncated Korteweg-de Vries (TKdV) equations, and uses a combination of computational, statistical, and analytical tools. In subsequent work, Majda and Qi (2019) analyzed more severely truncated systems—as low as two interacting modes—that exhibit a statistical phase transition to anomalous statistics and the creation of extreme events while enjoying a more tractable structure. More recently, Qi and Majda (2020) demonstrated the capability of machine learning strategies to accurately predict these extreme events. That work employs a deep neural network coupled with a judicious choice of the entropy loss function that emphasizes the dominant structures of the turbulent field Qi and Majda (2020). It should be noted that in these studies, extreme events are represented by strong skewness of the wavefield. They occur intermittently and on a relatively frequent basis, which is in contrast to the simpler situation of isolated, rare events (Guth and Sapsis 2019).

The purpose of the present manuscript is to provide a more comprehensive treatment of the *combined* experimental and theoretical efforts of Bolles et al. (2019) and Majda et al. (2019), Majda and Qi (2019). We present a variety of new findings that have resulted from a synergetic interaction between theory and experiments—a cooperative strategy with a proven record of success (Camassa et al. 2012; Ristroph et al. 2012; Ganedi et al. 2018). The outline of the paper is as follows. In Sect. 2, we detail the laboratory experiments of Bolles et al. (2019) and summarize previously reported findings on anomalous statistics of the surface displacement. We also present new experimental data on surface *slope* statistics—a line of inquiry motivated by the theoretical advancements of Majda et al. (2019), specifically the central role played by the slope in the Hamiltonian structure of TKdV. Section 3 discusses the TKdV theoretical framework, including both the deterministic and the statistical mechanics perspectives. In this section, we flesh out details of the nondimensionalization, which, for brevity, were only briefly discussed in the previous work. This exercise provides a more precise link between model and experimental parameters, ultimately facilitating a closer comparison between the two. We then discuss TKdV as a deterministic dynamical system, approachable from the viewpoint of statistical mechanics. The later perspective is based on the Hamiltonian structure and novel ensemble distributions that incorporate canonical and micro-canonical aspects (Abramov et al. 2003).

Section 4 presents a systematic comparison between experiments and theory, focusing on both surface displacement and surface slope. We find the statistical distributions of these two quantities to agree well across experiments and theory. In particular, we find remarkably quantitative agreement in the displacement statistics. We then examine numerical simulations of the TKdV deterministic dynamics, which elucidates the length and timescales required for statistical transitions in the experiments. Finally, this section discusses a peculiar power-law relationship between surface-displacement skewness and surface-slope variance predicted by the statistical mechanics framework (Majda et al. 2019). New experimental measurements conclusively confirm this prediction, further demonstrating the predictive power of the TKdV framework developed by Majda et al. (2019). We close with some final remarks in Sect. 5.

2 The Experiments

As diagrammed in Fig. 1a, the experiments consist of a long, narrow wave tank (6-m long × 20-cm wide × 30-cm high), with waves generated by a plexiglass paddle at one end (Bolles et al. 2019). The waves propagate through the tank and, roughly midway

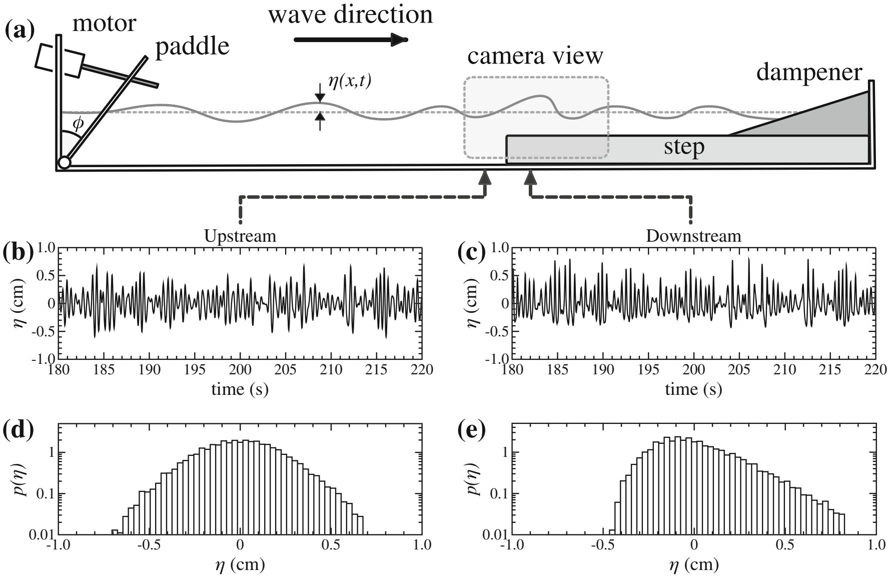

Fig. 1 **a** Experimental schematic: randomized waves are generated by a pivoting paddle and propagate over a step in bottom topography. **b**, **c** Surface displacement measured at representative locations upstream and downstream of the abrupt depth change (ADC). **d**, **e** Corresponding histograms showing symmetric upstream statistics and highly skewed downstream statistics. Figure adapted from Bolles et al. (2019)

through, pass over an abrupt depth change (ADC) created by a plexiglass step. The waves continue to propagate through the shallower depth until reaching the far end of the tank, at which point their energy is dissipated by a horse-hair dampener. Since the dampener minimizes backscatter, the waves in this experiment propagate primarily in one direction, from left to right in Fig. 1a.

The pivoting motion of the paddle is driven by a 5-phase stepper motor. To generate a randomized wavefield, the paddle angle ϕ is specified by a psuedo-random signal

$$\phi(t) = \phi_0 + \Delta\phi \sum_{n=1}^{N} a_n \cos(\omega_n t + \delta_n)\,, \tag{1}$$

$$a_n = \sqrt{\frac{2\Delta\omega}{\pi^{1/2}\sigma_\omega}}\ \exp\left(-\frac{(\omega_n - \omega_0)^2}{2\sigma_\omega^2}\right) \tag{2}$$

The angular frequencies are evenly spaced $\omega_n = n\Delta\omega$ with step size $\Delta\omega = (\omega_0 + 4\sigma_\omega)/N$, where ω_0 and σ_ω represent the mean and the bandwidth of ω, respectively. As in prior work, all experiments reported here use the values $\omega_0 = \sigma_\omega = 12.5$ rad/s, corresponding to a peak forcing frequency of 2 Hz and bandwidth of 2 Hz. The phases δ_n are uniformly distributed random variables, which results in a randomized wave train. The standard deviation of the paddle angle, $\Delta\phi$, controls the overall amplitude of the waves. In a single experiment, $\Delta\phi$ is fixed, and we will present a series of experiments with $\Delta\phi$ varied systematically.

The free surface is illuminated by light-emitting diodes and is imaged from the side-view with a Nikon D3300 at 60 frames per second. The illumination technique, coupled with high pixel count of the camera, allows surface displacements to be resolved with accuracy better than 1/3 millimeter. Furthermore, these optical measurements permit extraction of wave statistics *continuously* in space, rather than at a few discrete locations, which is crucial for identifying regions of anomalous wave activity. Further details of the experimental setup can be found in Bolles et al. (2019).

Example measurements of free surface displacements η are shown in Fig. 1b, c. These measurements are extracted from the images at two representative locations: one is a short distance (9 cm) upstream of the ADC and the other a short distance (15 cm) downstream. Both signals exhibit a combination of periodic and random behavior, with the dominant oscillations corresponding to the peak forcing frequency of 2 Hz.

The nature of the random fluctuations is revealed by the corresponding histograms shown in Fig. 1d, e on a semi-log scale. The upstream measurements are symmetrically distributed about the mean, $\eta = 0$. In fact, Bolles et al. (2019) found that these measurements follow a Gaussian distribution closely (Bolles et al. 2019). The downstream measurements, however, skew strongly toward positive displacement, $\eta > 0$. Bolles et al. (2019) found these measurements to be well described by a mean-zero gamma distribution (Bolles et al. 2019). The slower decay of the gamma distribution indicates an elevated level of extreme surface displacement, i.e., rogue waves. Bolles et al. (2019) estimated that a rogue wave can be up to 65 times more likely in these experiments than if displacements were Gaussian (Bolles et al. 2019).

The paddle amplitude in Fig. 1 is $\Delta\phi = 1.38°$, and this value was varied systematically in the range $\Delta\phi = 0.125°$–$2°$ to probe the different regimes of wave behavior, from linear to strongly nonlinear waves. Figure 2 shows long-time statistics of both surface displacement η and the surface slope η_x as they vary in space for six different driving amplitudes (see legend).

In this paper, we only examine statistic of mean-zero quantities, and so, for an arbitrary mean-zero quantity q, we have the following definitions

$$\mathrm{std}(q) = q_{\mathrm{std}} = \sqrt{\langle q^2 \rangle} \qquad \text{standard deviation} \tag{3}$$

$$\mathrm{skew}(q) = \left\langle q^3 \right\rangle / q_{\mathrm{std}}^3 \qquad \text{skewness} \tag{4}$$

$$\mathrm{kurt}(q) = \left\langle q^4 \right\rangle / q_{\mathrm{std}}^4 - 3 \qquad \text{(excess) kurtosis} \tag{5}$$

where $\langle\rangle$ indicates a mean—here a long-time mean at a fixed spatial location. Hereafter, we will simply refer to the excess kurtosis as kurtosis.

Figure 2 shows how these statistics vary in the vicinity of the ADC, located at $x = 0$, for both displacement and slope. First, the standard deviation of displacement, η_{std}, gives the coarsest possible estimate for the amplitude of waves. Figure 2a shows that while η_{std} increases with driving amplitude, it remains relatively uniform in space for each individual experiment, indicating that the overall amplitude of the wave train is not significantly altered by the presence of the ADC. The skewness and kurtosis, however, respond strongly to the ADC as long as the amplitude is sufficiently high. As seen in Fig. 2b, c, both the skewness and kurtosis are relatively small upstream of the

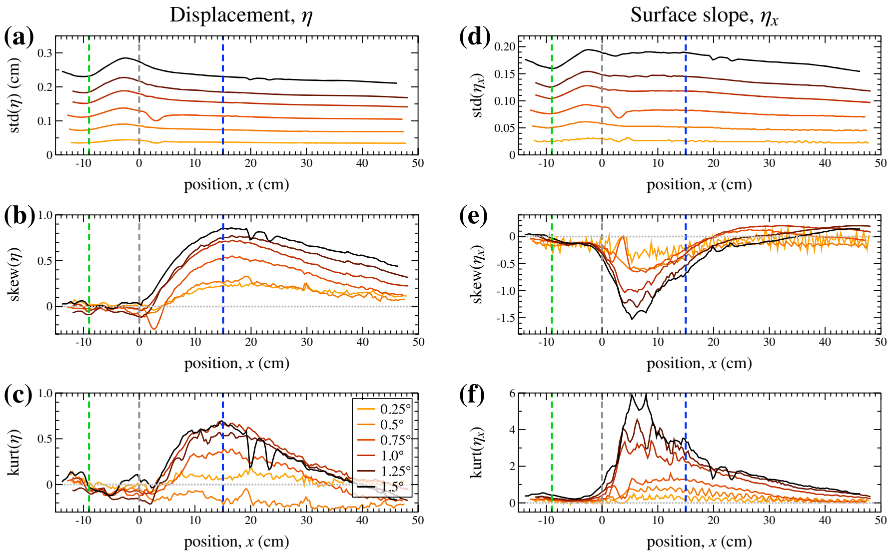

Fig. 2 Wave statistics as they vary in space for several experiments of different driving amplitudes (see legend). **a**–**c** Standard deviation, skewness, and kurtosis of the surface displacement η. **d**–**f** The same for surface slope η_x. **a** η_{std}, which sets a scale for wave amplitude, does not vary significantly crossing the ADC. **b**, **c** Skewness and kurtosis of η, however, show a strong response to the ADC. **d**–**f** The measurements of surface slope, η_x, are negatively skewed and also exhibit large kurtosis downstream of the ADC

ADC, indicating nearly Gaussian statistics, but then increase dramatically downstream and reach a peak near $x = 15$ cm. Interestingly, the location of the peak is the same for skewness and kurtosis and is insensitive to driving amplitude. The maximum values of skewness and kurtosis (approximately 0.9 and 0.7, respectively) seen in the figure indicate a significant departure from Gaussian statistics, as is constant with the histogram in Fig. 1e. Bolles et al. (2019) found that, once a threshold driving amplitude is exceeded (roughly $\Delta\phi = 0.5°$), the displacement statistics in this anomalous region are robustly described by the gamma distribution across all of the experiments. We note that we have gathered data for 15 different driving amplitudes, but only display 6 of those in Fig. 2 to avoid clutter.

To complement the displacement statistics, we report here statistics for the surface slope η_x in the right column of Fig. 2. Our attention to slope statistics was motivated by new theoretical developments by Majda et al. (2019), as will be expanded upon in later sections. We extract the surface slope by numerical differentiating images of the free surface using Savitzky-Golay smoothing filters. This ability to extract surface slope is another advantage of our optical measurements over the more commonly used technique of placing a set of discrete wave probes in the tank. As seen in Fig. 2a, the standard deviation of slope behaves similar to displacement: std(η_x) increases with driving amplitude, but remains nearly uniform in space for each individual experiment and is not affected by the ADC. The higher-order moments, however, respond strongly to the ADC if the driving amplitude is sufficiently high. The skewness of slope becomes highly negative and reaches a minimum near $x = 8$ cm, which is downstream of the

Table 1 Table of parameters

Description	Notation	Experimental range	'Representative' values
Peak forcing frequency	f_p	2 Hz	2 Hz
Characteristic amplitude	η_{std}	0.03–0.3 cm	0.21 cm
Upstream depth	d_-	12.5 cm	12.5 cm
Downstream depth	d_+	2.2–5.3 cm	3 cm
Upstream wavelength	$\lambda_- = \sqrt{gd_-}/f_p$	55 cm	55 cm
Downstream wavelength	$\lambda_+ = \sqrt{gd_+}/f_p$	23–36 cm	27 cm
Amplitude-to-depth ratio	$\varepsilon_0 = \eta_{\text{std}}/d_-$	0.0024–0.024	0.017
Depth-to-wavelength ratio	$\delta_0 = d_-/\lambda_-$	0.23	0.23
Depth ratio	$\mathcal{D}_+ = d_+/d_-$	0.18–0.42	0.24

ADC but upstream of the position where the displacement statistics peak. The kurtosis of η_x reaches a peak at nearly the same location as skewness. We note that the large *negative* skewness of η_x indicates a bias toward negative slope, which is consistent with a right-moving wave of steep leading surface and shallower trailing surface, i.e., a wave that is near overturning.

To have a simple baseline for comparison against theory, we refer to the data from Fig. 1 as the *reference* experiments. In these experiments, the driving amplitude is $\Delta\phi = 1.38°$ (intermediate between the two largest amplitudes shown in Fig. 2), the upstream depth is $d_- = 12.5$ cm, and the downstream depth is $d_+ = 3$ cm, giving a depth ratio of $\mathcal{D}_+ = d_+/d_- = 0.24$. From the data represented in Fig. 2, we extract a characteristic wave amplitude for the representative experiments of $\eta_{\text{std}} = 0.21$ cm, which will be important for setting dimensionless parameters that enter the theory. Table 1 lists the range of experimental parameters and the representative values, as well as values of dimensionless parameters that will be introduced later.

3 Theoretical Framework

We now introduce the theoretical framework that will be used to understand and quantify the experimental observations. This framework is based on a Galerkin truncation of the variable-depth Korteweg-de Vries (KdV) equation. The KdV equation is a well-established model for describing the propagation of unidirectional, shallow-water waves, accounting for weak nonlinearity and weak dispersion over long timescales and large spatial scales. We will perform Galerkin truncation of KdV to obtain a finite-dimensional dynamical system that exhibits weak turbulence. We outline the Hamiltonian structure of both the traditional KdV and the truncated systems. This structure is exploited to obtain invariant measures of the underlying dynamics and, ultimately, to rationalize the experimental findings on anomalous wave statistics triggered by an ADC.

3.1 The Korteweg-de Vries Equation with Variable Depth

We consider the surface displacement $\eta(x, t)$ of unidirectional, shallow-water waves in a reference frame moving with the characteristic wave speed, $\xi = x - ct$. Here, $c = \sqrt{gd}$ is the leading-order approximation to the wave speed (i.e., from linear theory), where g is gravity and d is the local depth. The leading-order dynamics are corrected to first order in small amplitude by the Korteweg-de Vries equation (KdV), which in dimensional form is given by Whitham (2011)

$$\eta_t + \frac{3c}{2d}\eta\eta_\xi + \frac{cd^2}{6}\eta_{\xi\xi\xi} = 0. \tag{6}$$

Motivated by the experiments, we consider waves that originate from a region of constant depth, encounter an abrupt depth change, and continue into another region of constant depth. Thus, depth will be piecewise constant

$$d = \begin{cases} d_- & \text{if } x < 0 \\ d_+ & \text{if } x > 0 \end{cases} \tag{7}$$

Most often, we consider waves moving into shallower depth, so that $d_- > d_+$. Throughout this paper, we use the subscript '$-$' and to represent upstream variables and '$+$' for downstream variables.

In the experiments, the randomized incoming wavefield is generated with a peak forcing frequency of $f_p = 2$ Hz, which gives rise to the characteristic wavelength of $\lambda = c/f_p = \sqrt{gd}/f_p$. Note that, both the characteristic wave speed $c = c_\pm$ and wavelength $\lambda = \lambda_\pm$ take different values upstream and downstream of the ADC. We remark that experimental measurements indicate that η_{std} is nearly the same on both sides of the ADC. Hence, we will not distinguish between upstream and downstream values of η_{std}.

3.2 Nondimensionalization and Relation to Experimental Scales

In this section, the variable-depth KdV equation (6) will be recast into a dimensionless form that is chosen for convenience in working with the statistical-mechanics framework of Majda et al. (2019). Since the choice of normalization is not unique, it is instructive to first introduce a generic normalization to facilitate comparison with other possible choices. To this end, we consider characteristic scales, $\mathcal{A}$, $\mathcal{L}$, $\mathcal{T}$ for the wave amplitude, longitudinal length, and time, respectively, which can remain unspecified for the moment. We introduce the dimensionless variables

$$u = \eta/\mathcal{A} \qquad \text{dimensionless surface displacement} \tag{8}$$

$$\tilde{x} = (x - ct)/\mathcal{L} \qquad \text{dimensionless position (in moving frame)} \tag{9}$$

$$\tilde{t} = t/\mathcal{T} \qquad \text{dimensionless time} \tag{10}$$

Recasting (6) in terms of these variables gives the generic dimensionless KdV equation:

$$u_t + \frac{3}{2}\left(\frac{c\mathcal{T}\mathcal{A}}{\mathcal{L}d}\right) u u_x + \frac{1}{6}\left(\frac{c\mathcal{T}d^2}{\mathcal{L}^3}\right) u_{xxx} = 0 \tag{11}$$

We have dropped the tilde notation above for simplicity and will henceforth use tildes only in cases of possible ambiguity.

Now, it is possible to choose the scales $\mathcal{A}$, $\mathcal{L}$, $\mathcal{T}$ for ease in working with a particular framework. We make the following choices,

$$\mathcal{A} = \pi^{1/2}\,\eta_{\text{std}}\,, \qquad \mathcal{L}_\pm = \frac{N\lambda_\pm}{2\pi}\,, \qquad \mathcal{T}_\pm = \frac{N\lambda_\pm}{2\pi f_p d_\pm} \tag{12}$$

where N is an integer to be chosen later. The explanation for these choices is as follows. First, we have chosen the characteristic amplitude, $\mathcal{A}$, to normalize the energy of the state-variable u to unity, as will be demonstrated in Sect. 3.4. Second, regarding $\mathcal{L}$, recall that λ is the characteristic wavelength corresponding to the peak forcing frequency f_p in the experiments. If only integer multiples of f_p were imposed (e.g., lower frequencies were not present), then the forcing would produce waves that are periodic over lengthscale λ. Since lower frequencies do exist, strict periodicity is not satisfied, but rather waves may be nearly periodic over the physical domain $\xi \in [-\lambda/2, \lambda/2]$. The approximation of near-periodicity becomes more accurate if integer multiples are considered, i.e., $\xi \in [-N\lambda/2, N\lambda/2]$. Thus, we have chosen $\mathcal{L}$ above so that, over the dimensionless domain $\tilde{x} \in [-\pi, \pi]$, periodic boundary conditions can be imposed on u with an accuracy that increases with N.

Lastly, regarding the characteristic timescale $\mathcal{T}$, the most basic timescale in the experiments is simply f_p^{-1}, i.e., the period of waves passing a fixed reference point. Of course, the leading-order behavior in shallow water is simply wave propagation with uniform speed c, i.e., no dispersion. The KdV equation provides the first correction to this behavior and describes dynamics that evolve over longer timescales. Hence, we have rescaled f_p^{-1} by the factor $N\lambda/(2\pi d) \gg 1$, which provides a suitably long timescale in line with other normalizations (Johnson 1997). The scales $\mathcal{L} = \mathcal{L}_\pm$ and $\mathcal{T} = \mathcal{T}_\pm$ change value across the ADC, which is important to note when comparing the theory against experimental measurements.

With the above choices, the dimensionless KdV equation takes the form

$$u_t + C_3\mathcal{D}^{-3/2}\, u u_x + C_2\mathcal{D}^{1/2}\, u_{xxx} = 0 \qquad \text{for } x \in [-\pi, \pi] \tag{13}$$

$$C_3 = \frac{3}{2}\pi^{1/2}\varepsilon_0\delta_0^{-1}\,, \quad C_2 = \frac{2\pi^2\delta_0}{3N^2} \tag{14}$$

The constants C_3 and C_2 do *not* change value crossing the ADC and are given in terms of the dimensionless parameters

$$\varepsilon_0 = \eta_{\mathrm{std}}/d_- \qquad \text{upstream amplitude-to-depth ratio} \tag{15}$$

$$\delta_0 = d_-/\lambda_- \qquad \text{upstream depth-to-wavelength ratio} \tag{16}$$

The reason for the subscripts 3 and 2 will become evident in the next section.

Meanwhile, the dimensionless depth $\mathcal{D} = d/d_-$ *does* change value across the ADC since the depth d changes. Recall that the reference frame of (13) moves with the local wave speed via the variable $\xi = x - ct$ from (6). Thus, the ADC is met at some time T_{ADC}, and for simplicity, we set $T_{ADC} = 0$. Therefore, we can regard $\mathcal{D}$ as a piecewise-constant function of dimensionless time

$$\mathcal{D} = \begin{cases} 1 & \text{for } t < 0 \\ \mathcal{D}_+ = d_+/d_- & \text{for } t > 0 \end{cases} \tag{17}$$

See Table 1 for a summary of these dimensionless parameters and their values in experiments.

A few comments are in order. First, we note that the original formulation of this theory utilized a slightly different normalizations (Majda et al. 2019), with identical powers of $\mathcal{D}$ in (13) but with different expressions for the other dimensionless parameters. These differences are purely cosmetic, and we have made the choices above simply to facilitate comparison with experiments. Second, an alternate formulation of the variable-depth KdV equation has been proposed in which the product $d^{1/4}\eta$, rather than η, is conjectured to vary continuously across the ADC (Johnson 1997). Of course, that assumption implies a discontinuity in surface displacement, which, though perhaps small, would be physically unrealistic. We have chosen to enforce continuity of surface displacement on the basis of physical realism. Furthermore, our *direct experimental measurements* of η_{std} give no indication of a significant change across the ADC, thus supporting the formulation used here. We note, however, that the only modification resulting from the alternate formulation would be in the power of $\mathcal{D}$ in the second term of (13): the power $\mathcal{D}^{-3/2}$ would become $\mathcal{D}^{-7/4}$. Thus, in this alternate formulation, the second term in (13) would be scaled by a negative power of $\mathcal{D}$ and the third term by exactly the same positive power of $\mathcal{D}$. Hence, the two formulations are qualitatively very similar with only slight quantitative differences expected.

3.3 Hamiltonian Structure of KdV

The variable-depth KdV (13), though not Hamiltonian throughout the entire domain, admits a Hamiltonian structure on each side of the ADC. Indeed, (13) can be expressed as

$$\partial_t u = \mathcal{J}\frac{\delta \mathcal{H}^{\pm}}{\delta u} \tag{18}$$

where $\mathcal{J} = \partial_x$ is the symplectic operator and $\mathcal{H} = \mathcal{H}^{\pm}$ is the Hamiltonian, which takes different forms on either side of the ADC. It is convenient to decompose the Hamiltonian into a so-called cubic and quadratic component, given, respectively, by

$$\mathcal{H}_3 = \frac{1}{6}\int_{-\pi}^{\pi} u^3 \mathrm{d}x\,, \qquad \mathcal{H}_2 = \frac{1}{2}\int_{-\pi}^{\pi} u_x^2 \mathrm{d}x\,. \tag{19}$$

Then, the Hamiltonian can be expressed as

$$\mathcal{H}^{\pm} = C_2 \mathcal{D}_{\pm}^{1/2}\,\mathcal{H}_2 - C_3 \mathcal{D}_{\pm}^{-3/2}\,\mathcal{H}_3 \tag{20}$$

where $\mathcal{D} = \mathcal{D}_{\pm}$ changes value across the ADC. More explicitly, substituting (17) gives the separate upstream and downstream Hamiltonians as

$$\mathcal{H}^{-} = C_2\,\mathcal{H}_2 - C_3\,\mathcal{H}_3 \qquad \text{for } t < 0 \tag{21}$$

$$\mathcal{H}^{+} = C_2 \mathcal{D}_{+}^{1/2}\,\mathcal{H}_2 - C_3 \mathcal{D}_{+}^{-3/2}\,\mathcal{H}_3 \qquad \text{for } t > 0 \tag{22}$$

As seen in (19), the cubic component, $\mathcal{H}_3$, represents the skewness of the wavefield, while the quadratic component, $\mathcal{H}_2$, represents the energy of the surface slope. The sign difference between the two in (20) thus represents a competition between wave skewness and slope energy. In particular, the appearance of the slope energy in the theory motivated the new experimental measurements on surface *slope* statistics reported in this paper.

We remark that in defining the Hamiltonian, we have chosen the sign convention of Lax (1975). More recent work of Bajars et al. (2013) and Majda et al. (2019) use a different convention, in which both the signs of $\mathcal{J}$ and $\mathcal{H}$ are opposite. Clearly, these sign differences cancel in (18) and thus the two conventions are completely equivalent. Using the second convention, Majda et al. (2019) found that a *negative* inverse temperature is required to accurately describe the experimental observations (Majda et al. 2019). We have chosen the convention above so that a *positive* inverse temperature may be used, allowing our theory to fit into the most conventional form of statistical mechanics.

We introduce two important invariants of KdV, namely the momentum and the energy

$$\mathcal{M}[u] \equiv \int_{-\pi}^{\pi} u \mathrm{d}x\ = 0, \qquad \mathcal{E}[u] \equiv \frac{1}{2}\int_{-\pi}^{\pi} u^2 \mathrm{d}x = 1 \tag{23}$$

As indicated above, the momentum of u vanishes since it is measured as displacement from equilibrium. Second, due to the choice of $\mathcal{A}$ in (12), the energy has been normalized to unity.

3.4 Truncated KdV

We now introduce the truncated KdV (TKdV) system, which is the main focus of the present study. Consider the state variable represented as a spatial Fourier series

$$u(x,t) = \sum_{k=-\infty}^{\infty} \hat{u}_k(t)\, e^{ikx}\,, \tag{24}$$

$$\hat{u}_k(t) = \frac{1}{2\pi}\int_{-\pi}^{\pi} u(x,t)\, e^{-ikx}\mathrm{d}x\,, \tag{25}$$

where $\hat{u}_k(t) \in \mathbb{C}$. Since $u(x,t)$ is real valued, $\hat{u}_{-k} = \hat{u}_k^*$, and since momentum vanishes $\hat{u}_0 = 0$. Next, consider the Galerkin truncation at wave number Λ

$$u_\Lambda(x,t) = \mathcal{P}_\Lambda u = \sum_{|k|\leq\Lambda} \hat{u}_k(t)\, e^{ikx}\,, \tag{26}$$

where $\mathcal{P}_\Lambda$ is a projection operator and (25) still holds. Inserting the projected variable, u_Λ, into the KdV equation and applying the projection operator, $\mathcal{P}_\Lambda$, again where necessary produces the truncated KdV equation (TKdV)

$$\frac{\partial u_\Lambda}{\partial t} + \frac{1}{2}C_3\mathcal{D}^{-3/2}\frac{\partial}{\partial x}\mathcal{P}_\Lambda(u_\Lambda)^2 + C_2\mathcal{D}^{1/2}\frac{\partial^3 u_\Lambda}{\partial x^3} = 0 \qquad \text{for } x \in [-\pi,\pi] \tag{27}$$

$$C_3 = \frac{3}{2}\pi^{1/2}\varepsilon_0\delta_0^{-1}\,, \quad C_2 = \frac{2\pi^2\delta_0}{3N^2} \tag{28}$$

Note that the additional projection operator in front of the quadratic term u_Λ^2, which removes the aliased modes of wavenumber larger than Λ. Since all wavenumbers larger than Λ have been removed, (27) represents a *finite* dimensional dynamical system, of dimension Λ over $\mathbb{C}$. The constants C_3 and C_2 are the same as before and have been repeated here for convenience.

Briefly, consider the parameter N, the number of characteristic wavelengths in the physical domain. We require $1 \leq N \leq \Lambda$, so that the mode $\hat{u}_N$, corresponding to the characteristic wavelength λ in the experiments, is resolved in the truncated dynamical system. If $N = \Lambda$, then λ corresponds to the smallest resolved wavelength. If instead N is chosen as an intermediate value between 1 and Λ, then the truncated system will resolve scales that are both bigger and smaller than the characteristic value λ.

Remarkably, the TKdV system (27) retains the Hamiltonian structure described in Sect. 3.3, with the only modification being the inclusion of the projection operator (Bajars et al. 2013; Majda et al. 2019). The piecewise defined Hamiltonian for TKdV is given by

$$\mathcal{H}_\Lambda^{\pm} = C_2\mathcal{D}_{\pm}^{1/2}\,\mathcal{H}_2[u_\Lambda] - C_3\mathcal{D}_{\pm}^{-3/2}\,\mathcal{H}_3[u_\Lambda] \tag{29}$$

where $\mathcal{H}_3$ and $\mathcal{H}_2$ are defined exactly as before (19), but now are simply applied to the projected variable $u_\Lambda = \mathcal{P}_\Lambda u$. Then, TKdV (27) can be expressed as

$$\partial_t u_\Lambda = \partial_x \mathcal{P}_\Lambda \frac{\delta \mathcal{H}_\Lambda^\pm}{\delta u_\Lambda} \tag{30}$$

where the truncated symplectic operator is $\mathcal{J}_\Lambda = \partial_x \mathcal{P}_\Lambda$.

The momentum and energy defined in (23) remain invariants of TKdV, with the same normalized values $\mathcal{M}[u_\Lambda] = 0$ and $\mathcal{E}[u_\Lambda] = 1$. Note that Parseval's identity implies

$$\mathcal{E}[u_\Lambda] = 2\pi \sum_{k=1}^{\Lambda} \left|\hat{u}_k\right|^2 = 1 \tag{31}$$

Thus, the dynamics of interest are confined to the unit hypersphere, $\mathcal{E} = 1$ in $\mathbb{C}^\Lambda$.

We comment on some important differences between the KdV and TKdV dynamical systems. Besides momentum, energy, and Hamiltonian, KdV possesses in infinite sequence of additional invariants (Lax 1975; Whitham 2011). Trajectories of KdV are therefore constrained by infinitely many conserved quantities, associated with the fact that it is a completely integrable system. The long-time dynamics of KdV are dominated by coherent structures, namely solitons. With finite truncation, however, the additional invariants cease to be conserved. The only known invariants of TKdV are the three mentioned already: momentum, energy, and Hamiltonian. Thus, finite truncation breaks integrability. Moreover, although soliton solutions are supported by TKdV, the long-time dynamics are not dictated by these structures. Rather, the finite truncation induces chaotic to weakly turbulent dynamics, as has been observed numerically (Bajars et al. 2013; Majda and Qi 2019). Stronger mixing is induced with energy cascades down and up scales.

In this way, the statistical theory developed herein differs from, and could likely complement, recent advances in the field of integrable turbulence (Zakharov 2009; Randoux et al. 2014; Costa et al. 2014; Randoux et al. 2016), where integrability is exploited to uncover certain statistical features of the system at hand. We remind the reader that KdV is asymptotically valid only for large spatial scales, and hence truncating the small scales does not alter the order of approximation made. In this sense, KdV and TKdV are on equal footing as far as physical realism—a more accurate framework would require either model closure to capture the small scale physics or else direct numerical simulation of the Euler equations. Where differences exist between KdV and TKdV, therefore, it is unclear *a priori* which model, if either, more closely resembles reality. This situation, of course, underscores the importance of controlled laboratory experiments.

3.5 Mixed Microcanonical-Canonical Gibbs Ensemble

In examining statistical mechanics of this Hamiltonian system, we will appeal to the idea of a *mixed microcanonical-canonical* Gibbs ensemble, as originally introduced by Abramov et al. (2003) for the Burgers-Hopf system. Specifically, this ensemble is microcanonical in energy and canonical in the Hamiltonian. The reason this ensemble is needed is the sign indefiniteness of the cubic term $\mathcal{H}_3$ in the Hamiltonian, which would cause a simple canonical distribution to diverge at infinity. The mixed ensemble, however, fixes the energy and hence confines dynamics to the compact set of the unit hypersphere $\mathcal{E} = 1$. Since the Hamiltonian is continuous, its value is bounded on the unit hypersphere, and thus the mixed ensemble produces a normalizable distribution. This construction applies equally well to the truncated or untruncated KdV system, and hence, we will not distinguish between the two. We note that other possible constructions may be applicable too (Kleeman and Turkington 2014).

On either side of the ADC, the mixed ensemble, or *Gibbs measure*, follows directly from the corresponding Hamiltonian via

$$\mathcal{G}^{\pm} = Z_{\beta^{\pm}}^{-1} \exp(-\beta^{\pm}\mathcal{H}^{\pm})\delta(\mathcal{E} - 1) \tag{32}$$

Here, $\beta = \beta^{\pm}$ is the inverse temperature, which will take a different values on either side of the ADC, and Z_β a constant that depends on β. Each measure $\mathcal{G}^{\pm}$ induces a corresponding ensemble average, denoted $\langle\cdot\rangle_{\pm}$.

We note that, in the current formulation, a positive inverse temperature $\beta > 0$ produces physically realistic statistics with a decaying energy spectrum, as is consistent with experiments (Majda et al. 2019; Bajars et al. 2013). Negative inverse temperature produces a physically unrealistic spectrum that has more energy at smaller scales. Hence, we will hereafter focus on the physically realistic case of $\beta > 0$. We also point out that a sufficient amount of nonlinear mixing is required for relaxation to the above Gibbs measure. In the linearized system, for example, modes propagate without interacting, and hence, the initial measure induced by the wave generator would remain unchanged.

3.6 Matching at the ADC

Recall that the abrupt depth change is met by traveling waves at dimensionless time $T_{ADC} = 0$, set to zero for convenience. The KdV equations describe wave dynamics over *long* timescales, physically $t \gg \mathcal{T}$, capturing weakly nonlinear and weakly dispersive effects. Meanwhile, evolution over shorter timescales is simply described by linear theory. The event of a wave crossing the ADC is precisely such a short-time event, and so we will employ the same matching conditions at the ADC that would result from linear theory.

More specifically, we assume continuity of the surface displacement, η, across the ADC (Whitham 2011; Rey et al. 1992). Since the propagation speed c changes with depth, waves crossing the ADC must rapidly adjust in wavelength in order to match the oscillation frequency just upstream of the ADC (Whitham 2011; Rey et al. 1992). The normalized domain $x \in [-\pi, \pi]$ is scaled on the characteristic wavelength and so there is no change in the dimensionless wavefield $u(x, t)$, giving the condition

$$u(x,t)|_{t=0^-} = u(x,t)|_{t=0^+}, \qquad \text{Deterministic matching condition} \tag{33}$$

We call (33) the deterministic matching condition to contrast with its statistical counterpart introduced below. This matching condition is employed in the deterministic simulations of TKdV (27). We note that in the alternate formulation mentioned earlier, it is the product $d^{1/4}\eta$ that would match at the ADC (Johnson 1997).

Now, from the perspective of statistical mechanics, consider the communication between the statistical ensembles, $\mathcal{G}^{\pm}$, upstream and downstream of the ADC. These two systems are in contact at the ADC, and so the upstream state with distribution $\mathcal{G}^{-}$ can be regarded as a thermal reservoir that influences the downstream distribution $\mathcal{G}^{+}$. In fact, the above deterministic condition directly leads to a simple description for the link. The quantity of interest is the outgoing Hamiltonian $\mathcal{H}^{+}$, since its value just upstream of the ADC, $t = 0^{-}$, is set by the incoming dynamics, and then this particular value is conserved thereafter in the outgoing dynamics. Since u matches at the ADC, so must $\mathcal{H}^{+}$, and, in fact, this matching holds for every individual trajectory. Recall that $\mathcal{H}^{+}(t)$ is not conserved in the upstream dynamics and so its value varies for $t < 0$. However, appealing to weak ergodicity, the ensemble mean $\left\langle \mathcal{H}^{+}(t) \right\rangle_{-}$ is expected to be independent of time. In particular, the value $\left\langle \mathcal{H}^{+}|_{t=0^{-}} \right\rangle_{-}$ is the same as the bare ensemble mean $\left\langle \mathcal{H}^{+} \right\rangle_{-}$. Afterwards, the particular value $\mathcal{H}^{+}|_{t=0^{-}}$ is conserved in the downstream dynamics, on a trajectory-by-trajectory basis and for all $t > 0$. Thus, the downstream measure $\mathcal{G}^{+}$ must recover the same ensemble mean $\left\langle \mathcal{H}^{+}|_{t=0^{-}} \right\rangle_{-} = \left\langle \mathcal{H}^{+} \right\rangle_{-}$, producing the simple condition

$$\left\langle \mathcal{H}^{+} \right\rangle_{-} = \left\langle \mathcal{H}^{+} \right\rangle_{+} \qquad \text{Statistical matching condition} \tag{34}$$

This statistical matching condition, originally derived by Majda et al. (2019), imposes a relationship between the two inverse temperatures β^{-} and β^{+}. In particular, we view β^{-} as given by the random state of the incoming wavefield. Thus, while we will treat β^{-} as a parameter that can be varied to study various possible system states, the downstream β^{+} is determined directly by the matching condition (34), giving the functional dependence

$$\beta^{+} = \mathcal{F}\left(\beta^{-}\right) \qquad \text{Transfer function} \tag{35}$$

The *transfer function* $\mathcal{F}$ will be a key link needed to relate the theory to experiments.

3.7 Numerical Computation of the Transfer Function

To compute the transfer function, we use a weighted random-sampling strategy. That is, we first sample the Fourier coefficients $\mathbf{u} = \left\{\hat{u}_k\right\}_{k=0}^{\Lambda}$ from a uniform distribution on the unit hypersphere $\mathcal{E} = 1$. The uniform sampling is achieved by first sampling from an isotropic Gaussian distribution and then normalizing to project onto the hypersphere (Abramov et al. 2003). These samples are then weighted by the appropriate Gibbs measure (32) to compute the expectations needed in the statistical matching condition (34). That is, for an arbitrary quantity Q, the ensemble expectation corresponding to

Hamiltonian $\mathcal{H}$ and inverse temperature β is numerically approximated as

$$\langle Q \rangle_\beta = \frac{\sum_{i=1}^{N_s} Q_i \exp(-\beta \mathcal{H}_i)}{\sum_{i=1}^{N_s} \exp(-\beta \mathcal{H}_i)} \tag{36}$$

where N_s is the number of samples. Then, enforcing the statistical matching condition (34) becomes a root-finding problem for the function

$$W(\beta^+) = \left\langle \mathcal{H}^+ \right\rangle_{\beta^+} - \left\langle \mathcal{H}^+ \right\rangle_{\beta^-} = 0 \tag{37}$$

Recall that we consider β^- as given, so that $\left\langle \mathcal{H}^+ \right\rangle_{\beta^-}$ is a constant that can be computed straightaway from (36). We then use the secant method with respect to the variable β^+ to find a root of $W(\beta^+)$ to the desired tolerance.

For simply computing the transfer function, this weighted-sampling approach offers significant advantages over more sophisticated methods, such as Markov Chain Monte Carlo (MCMC), in its ability to reuse the same samples of $\mathbf{u}$ for several different values of β^+. That is, we sample $\mathbf{u}$ from the uniform distribution and compute the list of Hamiltonian values only once, then simply vary β^+ in (37) with the secant method until the root is found. An MCMC method, on the other hand, would require the sampling to restart from scratch for each value of β^+, since the random steps in MCMC depend directly on the target distribution (32). We will, however, use MCMC to initialize direct numerical simulations of TKdV due to the superior efficiency for a single, given value of β.

3.8 Deterministic Simulations of TKdV

We now detail the method for direct numerical simulation of the TKdV dynamical system (27). In particular, since the conservation of energy and Hamiltonian plays a central role in the emergent statistical features of the system, it is important for the numerical scheme to conserve these quantities over long time horizons. We therefore employ a symplectic integrator, which, by preserving oriented areas in phase space, conserves the energy and Hamiltonian exactly.

Rearranging the TKdV system (27) gives

$$\frac{\partial u_\Lambda}{\partial t} = -\frac{1}{2} C_3 \mathcal{D}^{-3/2} \frac{\partial}{\partial x} \mathcal{P}_\Lambda (u_\Lambda)^2 - C_2 \mathcal{D}^{1/2} \frac{\partial^3 u_\Lambda}{\partial x^3} = F[u_\Lambda] \tag{38}$$

where we have represented the right-hand side by the operator $F[u_\Lambda]$. We employ a pseudo-spectral discretization of (38), with de-aliasing applied to the quadratic nonlinear term $\mathcal{P}_\Lambda(u_\Lambda)^2$ according to the standard 2/3-rule. That is, we first pad $\hat{u}_k$ with zeros for $\Lambda < |k| \leq 3\Lambda/2$, transform to physical space and square to obtain u_Λ^2 on a fine grid, then transform back to spectral space and truncate to obtain the Fourier coefficients of $\mathcal{P}_\Lambda(u_\Lambda)^2$. For simplicity, we denote these Fourier coefficients $\hat{v}_k$,

$$\mathcal{P}_\Lambda(u_\Lambda)^2 = \sum_{|k|\leq\Lambda} \hat{v}_k e^{ikx} \tag{39}$$

With this discretization, (38) can be recast in spectral space as a nonlinear ODE system

$$\frac{d}{dt}\hat{u}_k = -\frac{1}{2}C_3\mathcal{D}^{-3/2}\, ik\hat{v}_k + C_2\mathcal{D}^{1/2}\, ik^3\hat{u}_k = \hat{F}_k \tag{40}$$

The quadratic nonlinearity represented by $\hat{v}_k$ mixes the modes during evolution. We note the third-order linear term may become stiff for large Λ.

For time integration of (40), we employ a 4th-order midpoint symplectic scheme (McLachlan 1993). We introduce the spectral vectors $\mathbf{u} = \left\{\hat{u}_k\right\}_{k=0}^{\Lambda}$ and $\mathbf{F} = \left\{\hat{F}_k\right\}_{k=0}^{\Lambda}$, and let $\mathbf{u}^n$ denote the solution at time t_n. The midpoint method has two intermediate stages and the auxiliary vectors $\mathbf{y}_1, \mathbf{y}_2$:

$$\mathbf{y}_1 - \mathbf{u}^n = w_1\Delta t\,\mathbf{F}\left[\frac{1}{2}\left(\mathbf{y}_1 + \mathbf{u}^n\right)\right], \tag{41}$$

$$\mathbf{y}_2 - \mathbf{y}_1 = w_2\Delta t\,\mathbf{F}\left[\frac{1}{2}\left(\mathbf{y}_2 + \mathbf{y}_1\right)\right], \tag{42}$$

$$\mathbf{u}^{n+1} - \mathbf{y}_2 = w_3\Delta t\,\mathbf{F}\left[\frac{1}{2}\left(\mathbf{u}^{n+1} + \mathbf{y}_2\right)\right], \tag{43}$$

with the time increments $w_1 = \left(2 + 2^{1/3} + 2^{-1/3}\right)/3$, $w_2 = 1 - 2w_1$, and $w_3 = w_1$. The semi-implicit nature of (41)–(43) combined with the nonlinearity in $\mathbf{F}$ requires iteration. We split $\mathbf{F}$ into linear and nonlinear components, with the linear component being easily inverted since it is diagonal in spectral space. At each step of (41)–(43), we perform Picard iteration on the nonlinear component until convergence is achieved with a tolerance of $\delta = 1 \times 10^{-10}$. The starting guess for the iterations is determined by quadratic extrapolation from the previous three stages.

For the initial conditions, $\mathbf{u}^0$, of the direct numerical simulation, we sample from the upstream Gibbs ensemble $\mathcal{G}^-$ (32) with a prescribed inverse temperature β^-. We achieve this sampling via a Metropolis-Hasting Monte Carlo algorithm as detailed in Majda et al. (2019).

3.9 Scaling Analysis to Link Inverse Temperature to Experiments

Since the inverse temperature, β, is a key modeling parameter, it would be highly desirable to normalize the system such that the value of β does not depend sensitively on the truncation index as Λ grows large. That way, β can be interpreted as a real physical parameter that can be linked to the experiments and whose value does not depend sensitively on where one chooses to truncate the system. The one modeling parameter that is left to be set is N, which represents the number of characteristic wavelengths in the periodic domain. In what follows, we will determine reasonable constraints on N that allow β to be asymptotically independent of Λ.

The invariant measure exhibits the proportionality $\mathcal{G}_\Lambda \propto \exp(-\beta_\Lambda \mathcal{H}_\Lambda)$, where we have made explicit the dependence of all quantities on Λ. In particular, if $\mathcal{H}_\Lambda$ were to depend sensitively on Λ in expectation, then β_Λ would need to compensate in order to produce the same invariant measure. Hence, it would be desirable to scale the system in such a way that $\mathcal{H}_\Lambda$ does not depend sensitively on Λ, at least in expectation. To achieve this insensitivity, we will appeal to the uniform measure $\mathcal{G}_0$ and the idea of equipartition of energy (Abramov et al. 2003), since these two concepts afford simple scaling estimates.

Recall that $\mathcal{H}_\Lambda$ is composed of the cubic and quadratic components $\mathcal{H}_3$ and $\mathcal{H}_2$. Due to the odd symmetry of $\mathcal{H}_3$, it is easy to see that $\langle \mathcal{H}_3 \rangle_0 = 0$ with respect to the uniform measure $\mathcal{G}_0$. The quadratic component, however, requires closer inspection. Due to Parseval's identity, $\mathcal{H}_2$ can be written as

$$\mathcal{H}_2 = \frac{1}{2}\int_{-\pi}^{\pi} u_x^2 \mathrm{d}x = 2\pi \sum_{k=1}^{\Lambda} k^2 \left|\hat{u}_k\right|^2 \tag{44}$$

Due to the constraint $\mathcal{E}[u_\Lambda] = 1$, the equipartioned microstate is given by

$$\left|\hat{u}_k\right|^2 \approx \frac{1}{2\pi\Lambda} \qquad \text{for equipartition of energy} \tag{45}$$

Then, the expected value of $\mathcal{H}_2$ under the uniform measure is

$$\langle \mathcal{H}_2 \rangle_0 = 2\pi \sum_{k=1}^{\Lambda} k^2 \left\langle \left|\hat{u}_k\right|^2 \right\rangle_0 \sim \frac{1}{3}\Lambda^2 \tag{46}$$

where we have used the identity for the Gauss-like sum

$$\sum_{k=1}^{n} k^2 = \frac{1}{6} n(n+1)(2n+1) \approx \frac{1}{3} n^3 \tag{47}$$

Importantly, (46) shows that the expected value of $\mathcal{H}_2$ grows like Λ^2, which appears problematic for obtaining independence as $\Lambda \to \infty$. However, $\mathcal{H}_2$ enters $\mathcal{H}$ in product with the coefficient C_2, which itself scales as $C_2 \sim N^{-2}$. Hence, obtaining the desired asymptotic independence with respect to Λ simply requires that N grow proportionally to Λ, as was already argued on physical grounds in Sect. 3.4. Thus, any of the choices $N = \Lambda, \Lambda/2$, or $\Lambda/4$, discussed in that section would be valid. In particular, if $N = \Lambda$, then the characteristic wavelength in experiments corresponds to the smallest resolved wavelength in the dynamical system. It is perhaps more sensible to choose N to be an intermediate value between 1 and Λ, so that some scales both larger than and smaller than the characteristic wavelength λ are resolved. As default, we will choose $N = \Lambda/2$, so that on a log-scale, the characteristic wavelength lies directly in the middle of the resolved wavelengths.

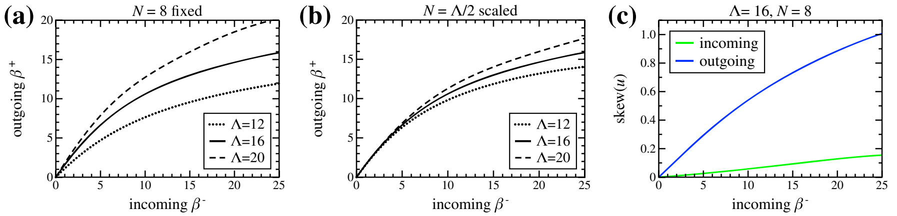

Fig. 3 Analysis of the transfer function, $\beta^{+} = \mathcal{F}\left(\beta^{-}\right)$, and calibration of the inverse temperature. **a**, **b** The transfer function for three values of Λ with either **a** $N = 8$ fixed or **b** $N = \Lambda/2$ scaled. Scaling N with Λ mitigates the sensitivity to Λ. **c** The incoming and outgoing skewness versus β^{-} implied by the matching condition. In line with experiments, the skewness is enhanced significantly in the outgoing wavefield

We note that the experiments discussed here preceded the development of the theory, and hence had no intent of mimicking a Gibbs measure in the wave forcing. We expect that if the experimental forcing were designed to mimic the Gibbs measure, in particular the precise spectral decay, then it would be more straightforward to assign a value to the model parameter N. We, however, leave that task for future research due to the significant cost of performing an entirely new set of experiments compared to the relative ease and great value in re-analyzing existing experimental data in light of the new theoretical developments.

4 Comparison Between Theory and Experiments

With the experimental setup described and the theory outlined, we now present results comparing the two. Unless stated otherwise, all parameters used in the theory are taken directly from their experimental values listed in Table 1.

4.1 Calibration of the Inverse Temperature

At this point, all parameters appearing in the theoretical model have been linked directly to experimental parameters with the exception of the inverse temperature of the incoming flow, β^{-}. Our strategy is to use the outgoing skewness as the main diagnostic to determine a realistic range for β^{-}. That is, for an input β^{-}, the downstream inverse temperature β^{+} is determined by (34), which ultimately sets the skewness of the outgoing wavefield.

Figures 3a, b show the transfer function $\beta^{+} = \mathcal{F}(\beta^{-})$ that results from the statistical matching condition (34), for an incoming inverse temperature in the range $0 \leq \beta^{-} \leq 25$. Figure 3a shows the cases $\Lambda = 12$, 16, and 20 with $N = 8$ fixed in each. In this figure, the transfer function changes significantly with Λ. Figure 3b shows the same but with the scaling $N = \Lambda/2$ that was argued in the previous section. In this figure, the three curves come much closer to one another. Thus, scaling N appropriately greatly mitigates the sensitivity of the transfer function to Λ, though it does not completely remove the dependence.

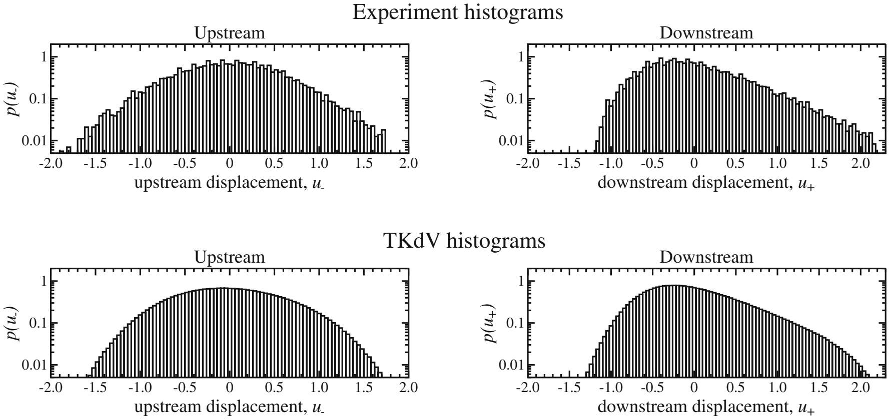

Fig. 4 Comparison of displacement histograms from experiment and theory. Upon calibrating the inverse temperature β^-, the TKdV simulations recover the experimentally measured distributions in remarkable detail. In particular, they exhibit the transition from a nearly symmetric distribution upstream to a highly skewed distribution downstream

Next, Fig. 3c shows the skewness of the incoming (green) and outgoing (blue) wavefields, as they depend on the incoming inverse temperature β^- for the case $(\Lambda, N) = (16, 8)$. In line with experimental observations, the incoming skewness is small, while the outgoing wave skewness is much higher. Specifically, to capture the experimentally observed peak skewness range of 0.6–0.9 seen for the larger amplitudes in Fig. 2b, requires selecting β^- in the range 10–25.

4.2 Statistical Comparison Between Theory and Experiments

We now aim to compare the wave statistics measured in experiments against those that emerge from the TKdV theory. Throughout, we will focus on the representative set of experiments detailed in Table 1, in which the peak downstream skewness was measured to be 0.83. With $(\Lambda, N) = (16, 8)$ fixed, Fig. 3c indicates $\beta^- = 20$ as a reasonable value to attain the desired skewness. We thus run the deterministic TKdV simulations with these model parameters and with ε_0, δ_0, and $\mathcal{D}_+$ set to the representative values in Table 1. We run the simulations to a sufficiently long dimensionless time of $t_f = 10$, with $dt = 5 \times 10^{-4}$, and with 10^3 trajectories sampled from the upstream Gibbs measure $\mathcal{G}^-$.

In Fig. 4, we show the distributions of surface displacement that were measured in the experiments (top row) versus those that emerge from the TKdV simulations (bottom row). The experimental histograms represent exactly the same data depicted in Fig. 1, only converted to dimensionless displacement, u, for comparison against theory. Meanwhile, the TKdV distributions are extracted from the long-time history of several trajectories sampled from the Gibbs ensemble, i.e., mixed long-time/ensemble histograms. All histograms are shown on a semi-log scale to facilitate comparison of the tails, where extreme events lie.

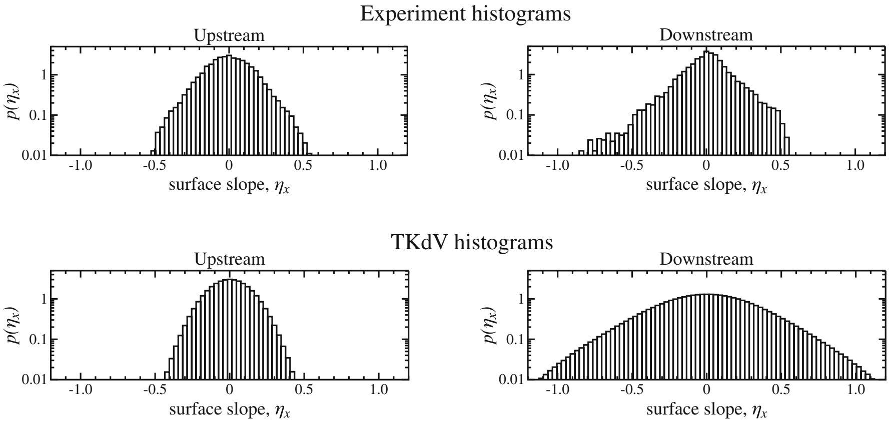

Fig. 5 Comparison of surface slope histograms. The experiments and TKdV simulations show very similar slope distributions upstream. Downstream, the theory accounts for the spread of the distribution and the long exponential tails, while differences in the detailed shape of the distributions are also visible. Note the elevated uncertainty in the experimental data due to numerical differentiation of free surface measurements

The comparison between experiments and theory in Fig. 4 is striking. As seen in the figure, both the experiments and theory show a transition from a nearly symmetric upstream distribution to a highly skewed distribution downstream. The TKdV theory not only captures this transition, but also recovers the shape of the resulting downstream distribution in remarkable detail. Nearly every feature that can be compared—the decay rate of the tail, the position and value of the peak, the rapid cutoff for negative u—matches surprisingly well. This comparison offers compelling visual evidence for: (a) the predictive power of the TKdV framework, and (b) the successful calibration of the incoming inverse temperature.

Next, we aim to make the same comparison for free surface slopes. We note that the derivative, $\partial\eta/\partial x$, is already a dimensionless quantity with a simple physical interpretation, namely the slope of the free surface, whereas the interpretation of $\partial u/\partial\tilde{x}$ is tied to the characteristic values $\mathcal{A}$ and $\mathcal{L}$. We therefore convert the theoretical calculated slopes values back to physical slopes via

$$\frac{\partial\eta}{\partial x} = 2\pi^{3/2}\frac{\eta_{\text{std}}}{\lambda_\pm}\frac{\partial u_\pm}{\partial\tilde{x}} \tag{48}$$

So that the peak experimental wavelength λ (corresponding to $f_p = 2$ Hz) would be mapped to the dominating TKdV spectral mode, $k = 1$, this conversion formula has not been corrected with the extra factor of N present in (12).

Figure 5 shows the distributions of surface slope that result from experiments (top) and theory (bottom). These histograms show intriguing similarities and differences. First, the upstream slope distribution is captured well by the TKdV simulations, both in its nearly symmetric shape and its scale. We note that while the standard deviation of displacement was input into the TKdV theory, the slope standard deviation was not. Downstream, both the experimental and theoretical slope distributions spread significantly. Interestingly, in the experiments, it is not the standard deviation that increases significantly upon crossing the depth change (std(η_x) increases from 0.15 to 0.17), but instead the excess kurtosis, which jumps from a value of 0.46 upstream to 3.4 downstream. Likewise, in the TKdV theory, std(η_x) grows from 0.13 upstream to 0.33 downstream, and kurt(η_x) grows from −0.04 to 0.50. Thus, the theoretically predicted jump in kurtosis, though not as extreme as that measured in experiments, is quite significant. These elevated levels of kurtosis are associated with the distinct appearance of the downstream distributions, most notably the long, flat tails that appear in both experiments and theory.

Differences in the detailed shapes of these downstream distributions are also visible. First, we point out that the experimental measurements involve numerical differentiation of surface displacement extracted from optical images, a process that unavoidably amplifies any noise that is present. We must therefore proceed with caution in comparing the experiment and theory, recognizing the possibility that observed discrepancies may be due to these measurement errors. Nonetheless, we notice that the theoretically predicted distributions remain symmetric downstream and the experimental ones skew toward negative slope. As mentioned in Sect. 2, negative skewness is consistent with a right-moving wave of steep leading surface (i.e., negative slope). Additionally, the peak of the experimental distribution appears sharper than in the theory.

4.3 Wave Dynamics and Analysis of Timescales

As a complement to the above statistical comparison, we now examine the wave dynamics of a few individual trajectories from the TKdV simulations. Figure 6 shows example upstream and downstream solution trajectories from the same TKdV simulations that were used to produce the histograms in Figs. 4, 5. The dimensionless displacement, u, is represented by color in the domain $(x, t) \in [-\pi, \pi] \times [-10, 10]$, where the ADC is encountered at $t = 0$.

Visual differences between the upstream and downstream dynamics are apparent in Fig. 6. The upstream trajectory shows several waves of moderate amplitude all propagating leftward. Here, the magnitude of the positive and negative displacements are comparable. This is in stark contrast to the downstream dynamics, which feature fewer waves of larger amplitude propagating in either direction. In particular, one large wave is seen to propagate from the lower-left corner of the figure to the upper right. A bias toward positive surface displacement is apparent in these downstream dynamics, without even viewing the histograms.

These observations can be rationalized with some simple observations regarding the structure of the TKdV system. Upstream of the ADC, since $\mathcal{D} = 1$, the nonlinear effects are relatively weak and the dynamics are dominated by dispersion. Linearizing (27) and introducing the ansatz $u_k = e^{i(kx-\omega_k t)}$ produce the dispersion relation for angular frequency $\omega_k = -C_2 k^3$, or for phase velocity $c_k = \omega_k / k = -C_2 k^2$ (Majda and Qi 2019). In particular, the phase velocity is strictly negative, implying that waves only propagate leftward, as is consistent with Fig. 6a.

Downstream of the ADC, however, the depth ratio changes to $\mathcal{D} = 0.24$. This change significantly amplifies nonlinearity while suppressing dispersion, and thereby

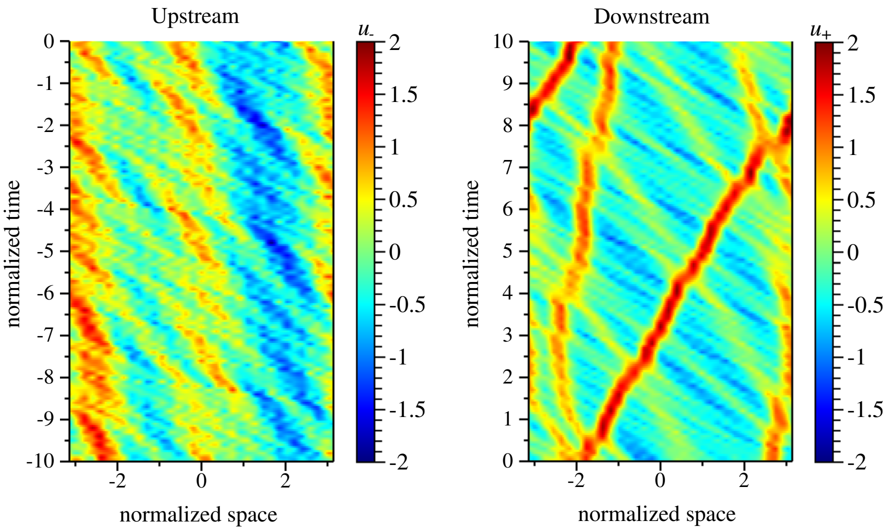

Fig. 6 Sample upstream and downstream solution trajectories from the same ensemble TKdV simulations featured in Figs. 4 and 5. The upstream solutions exhibit only leftward propagating waves and a high degree of regularity, while the downstream solutions exhibit both left and rightward moving waves along with more intermittency

allows waves to propagate in either direction. In particular, the dispersionless limit of KdV is the Burgers-Hopf equation, for which the nonlinear advection is proportional in both amplitude and direction to the value of u. Hence, positive displacements would be expected to move rightward, as is seen in Fig. 6b.

We remind the reader that the KdV framework tracks the long-time evolution of waves in a reference frame moving with the characteristic speed $c = \sqrt{gd}$ from linear theory. Hence, the above discussion of left-or-right going waves cannot be interpreted in the context of the experiments without an appropriate Galilean transformation. Thus, in the laboratory frame, all waves indeed propagate unidirectionally, from left to right, with a speed near c. The directions and speeds calculated by the TKdV framework simply quantify the deviation of the true wave speed from c.

Finally, Fig. 6 sheds light on the timescales required for wave evolution in the TKdV framework. It appears that the normalized time of $t = 10$ is approximately the correct timescale to observe substantial wave dynamics. More precisely, both the left-going waves in Fig. 6a and the right-going waves in Fig. 6b require a dimensionless time of about $t = 7$ to traverse the entire periodic domain. For the representative experiments, the characteristic timescale, $\mathcal{T}$, is 2.8 s upstream and 5.7 s downstream. Hence, a dimensionless time of $t = 7$ corresponds to 20 s and 40 s upstream and downstream, respectively. Given the wave speeds ($c = 110$ cm/s upstream and 54 cm/s downstream), these timescales can be converted to distances traveled by the waves. In fact, a simple calculation using the definitions in Sect. 3 gives the distance traveled as $7Ng/(2\pi f_p^2)$, which, due to a serendipitous cancellation, is independent of depth. Hence, the distance traveled by the waves over a dimensionless time of $t = 7$ is the same value upstream

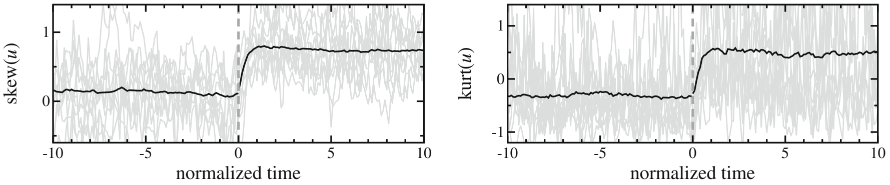

Fig. 7 Dynamic evolution of surface-displacement skewness and kurtosis from the TKdV simulations. Faint gray curves show skewness and kurtosis of 100 individual trajectories, and the bold black curves show the corresponding ensemble mean. Skewness and kurtosis evolve over much shorter timescales than that required for waves to cross the domain

and downstream, 22 m. Note that, this distance is significantly greater than the 6-meter length of the experimental wave tank.

These estimates raise an important question: if a distance of 22 m is required for significant wave evolution under the KdV framework, how do the experiments exhibit substantial changes in wave statistics a much shorter distance downstream of the ADC? The results shown in Fig. 7 help resolve this question. This figure shows the evolution of surface-displacement skewness (left) and kurtosis (right) computed by the same deterministic TKdV simulations as pictured in Fig. 6. The bold black curve shows the ensemble mean (ensemble size of 1000), while the faint gray curves show the skewness and kurtosis of 100 individual trajectories to give a sense for the variation involved. Importantly, the skewness and kurtosis evolve on a much shorter timescale than the aforementioned $t = 7$. More precisely, skewness and kurtosis have already saturated to their asymptotic value by $t = 1$, and reach half of that value by $t = 0.18$. These dimensionless times correspond to travel distances of 310 cm and 56 cm, respectively—much shorter than the previously mentioned 22 m, and on the same order as the relevant distances in the experiments. Thus, after crossing the ADC, the wavefield rapidly reconfigures itself enough to fundamentally alter its statistical distributions, and the timescale for this reconfiguration is much shorter than the time required for waves to cross the entire periodic domain.

4.4 Explicit Formula for Outgoing Skewness and Experimental Confirmation

We now discuss arguably the most novel single result of the manuscript. In the recent theoretical study, Majda et al. (2019) derived an explicit formula for the outgoing wavefield skewness in terms of the system parameters (Majda et al. 2019). More specifically, this formula relates the downstream skewness of surface displacement, $\mathrm{skew}(\eta)$, to the change in slope variance, $\mathrm{var}(\eta_x)$. Here, we recap the derivation of this formula and then test the prediction against new, direct experimental measurements.

The explicit formula for outgoing skewness arises directly from the statistical matching condition (34), which states that the downstream Hamiltonian must match in expected value at the ADC, i.e., with respect to the incoming and outgoing Gibbs measures. This condition can be written more explicitly as

$$C_2\mathcal{D}_+^{1/2}\ \langle\mathcal{H}_2\rangle_- - C_3\mathcal{D}_+^{-3/2}\ \langle\mathcal{H}_3\rangle_- = C_2\mathcal{D}_+^{1/2}\ \langle\mathcal{H}_2\rangle_+ - C_3\mathcal{D}_+^{-3/2}\ \langle\mathcal{H}_3\rangle_+ \quad (49)$$

Both the experiments and simulations show the upstream skewness to be negligible compared to its downstream counterpart, allowing the term with $\langle\mathcal{H}_3\rangle_-$ to be dropped in (49). With this approximation, (49) yields the relationship

$$\frac{\langle\mathcal{H}_3\rangle_+}{\langle\mathcal{H}_2\rangle_+ - \langle\mathcal{H}_2\rangle_-} = \frac{C_2}{C_3}\mathcal{D}_+^2 \tag{50}$$

Our next task is to convert this formula to physical variables so that it can be tested against experimental data. First, following the definition of $\mathcal{H}_3$ in (19) and the definition, $u = \eta/(\pi^{1/2}\eta_{\mathrm{std}})$, a straightforward calculation gives

$$\langle\mathcal{H}_3\rangle_+ = \frac{\pi}{3}\left\langle u^3\right\rangle_+ = \frac{1}{3\pi^{1/2}}\frac{\left\langle\eta^3\right\rangle_+}{\eta_{\mathrm{std}}^3} = \frac{1}{3\pi^{1/2}}\mathrm{skew}_+(\eta) \tag{51}$$

This equation expresses a direct relationship between the expected value of $\mathcal{H}_3$ and the outgoing skewness of surface displacement. Next, we must convert the $\mathcal{H}_2$-quantities, which involve surface slope. Using the definition of $\mathcal{H}_2$ in (19) and $\mathcal{L}_+$ in (12) gives

$$\langle\mathcal{H}_2\rangle_\pm = \pi\left\langle u_x^2\right\rangle_\pm = \left(\frac{N\lambda_+}{2\pi\,\eta_{\mathrm{std}}}\right)^2 \mathrm{var}_\pm(\eta_x) \tag{52}$$

We note that the downstream scale $\mathcal{L}_+$ is used in this conversion, since it is the downstream Hamiltonian that is matched in (34). This formula links the expected value of $\mathcal{H}_2$ to the variance of surface slope.

Inserting (51) and (52) into (50), and using the definitions of C_2 and C_3 from (14), gives the explicit formula

$$\frac{\mathrm{skew}_+(\eta)}{\mathrm{var}_+(\eta_x) - \mathrm{var}_-(\eta_x)} = \frac{1}{3}\varepsilon_0^{-3}\mathcal{D}_+^3 \tag{53}$$

This formula links the skewness of the outgoing wavefield to the change in the variance of surface slope. In particular, it predicts their ratio to scale as the *inverse cube of wave amplitude*, ε_0^{-3}, and the *cube of the depth ratio*, $\mathcal{D}_+^3$. It is a rather unexpected relationship, as it would have been difficult to anticipate that the displacement skewness and slope variance, among all possible variable combinations, are so intimately related.

Fortunately, it is a relationship that can be tested directly against the experimental measurements, specifically the type of data that was presented in Fig. 2. Formula (53) draws focus to the spatial variation of displacement skewness, which we replot for convenience in Fig. 8a, and the variance of surface slope, shown in Fig. 8b. To test (53), we must select a representative downstream position to evaluate $\mathrm{skew}_+(\eta)$ and $\mathrm{var}_+(\eta_x)$, and a representative upstream position for $\mathrm{var}_-(\eta_x)$. In short, we select the same representative locations used to evaluate the histograms in Figs. 1, 4, and 5, namely $x = 15$ cm downstream and $x = -9$ cm upstream. These positions are indicated by the blue and green vertical dashed lines in Fig. 8a, b. Recall

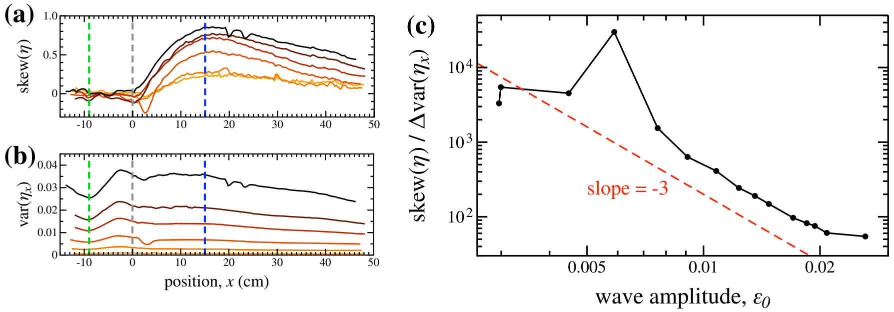

Fig. 8 Experimental confirmation of the explicit formula for outgoing skewness (53). **a**, **b** Spatial variation of skew(η) and var(η_x) for several different amplitudes. The maximum of skew(η) and the minimum of var(η_x) each occur at a location that is insensitive to amplitude, x =15 cm (blue) and -9 cm (green), respectively. **c** Measurements of the ratio skew(η)/Δvar(η_x) from 15 different experiments plotted against the dimensionless wave amplitude ε_0. For sufficiently large amplitude, the measurements follow the predicted ε_0^{-3} power law closely

that $x = 15$ cm corresponds to the peak of the downstream skewness and kurtosis. Meanwhile, we see in Fig. 8b that $x = -9$ cm corresponds to a slight dip in var(η_x).

With these locations selected, we evaluate the ratio skew(η)/Δvar(η_x) for each experiment and plot the result against dimensionless wave amplitude, $\varepsilon_0 = \eta_{\text{std}}/d_-$ on a log-log scale in Fig. 8c. While the data show significant variation at small amplitudes, it shows a well-defined decreasing trend at larger amplitudes. In particular, the decay rate of the ratio, skew(η)/Δvar(η_x) $\sim \varepsilon_0^{-3}$, is well predicted by the explicit formula (53), shown by the red dashed line in Fig. 8c. The apparently less predictable behavior at small amplitudes can be attributed to the fact that, in order for the system to relax to the Gibbs measure, modes must interact through nonlinearity. For the smallest amplitude experiments, the amount of nonlinearity is apparently too small for modes to mix sufficiently.

We remark that Eq. (53) bears similarity to a formula derived by Onorato and Suret (2016), in the context of *constant-depth* KdV, that relates variations in skewness to variations in spectral bandwidth. Indeed, since $\eta_t \approx c\eta_x$ to leading order, the term var(η_x) in Eq. (53) could be interpreted as approximately the spectral bandwidth. We note that an analogous formula has been derived for the nonlinear Schrödinger equation relating kurtosis to bandwidth variations (Onorato et al. 2016). The present study differs in that it predicts a moment-bandwidth relation for waves propagating over *variable* depth, where it is the depth change that creates system disequilibrium. A small transition region connects two near-equilibrium systems, i.e., one far upstream and one far downstream. The link between these two equilibrium states is made mathematically precise by the statistical matching condition (34), which is the key ingredient needed to derive Eq. (53). This is in contrast to the simpler situation of waves propagating over constant depth, where spectral variations and the associated moment variations arise from out-of-equilibrium initial conditions (Onorato and Suret 2016; Onorato et al. 2016).

5 Concluding Remarks

This manuscript extends the parallel experimental and modeling efforts of Bolles et al. (2019) and Majda et al. (2019) concerning the emergence of anomalous wave statistics from abrupt changes in bottom topography. The theoretical framework is based on deterministic and statistical analysis of the TKdV system, with exploitation of the Hamiltonian structure and the associated invariant Gibbs measures. The theory depends crucially on matching the incoming and outgoing invariant measures at the abrupt depth change, so as to link the incoming and outgoing states. Throughout, we have emphasized the synergy between the experiments and theory, with experimental data informing theoretical advancements and model predictions motivating new experimental measurements.

Careful calibration of the inverse temperature against the experimental data allowed for a detailed comparison between experimental and theoretically predicted wave statistics. The outgoing distributions of surface displacement predicted by the TKdV framework capture in remarkable detail the experimental measurements. We have extended this statistical analysis to surface slope, a line of inquiry motivated by the importance of $\mathcal{H}_2$, the slope standard deviation, in the theory. The comparison of slope statistics shows intriguing similarities, while also some quantitative differences in the shape and skewness of the outgoing distributions.

Finally, Majda et al. (2019) derived an explicit formula for the skewness of the outgoing wavefield, which we have tested against direct experimental measurements. Specifically, the formula predicts how the ratio of displacement skewness to slope variance, $\text{skew}(\eta)/\Delta\text{var}(\eta_x)$, depends on wave amplitude. The experimental measurements conclusively confirm the inverse-cube dependence on wave amplitude, thus highlighting the predictive power of the TKdV statistical mechanics framework.

We note that since the ratio, $\text{skew}(\eta)/\Delta\text{var}(\eta_x)$, exhibits such a clear dependence on input parameters, it could prove a useful diagnostic for anomalous wave observations in the ocean. In particular, this quantity seems to provide a signature for anomalous waves that are triggered by abrupt depth changes. Examination of this ratio in field data is an exciting avenue for future research.

Acknowledgements C.T.B. acknowledges support from the IDEA grant at Florida State University, as well as from the Geophysical Fluid Dynamics Institute. M.N.J.M. acknowledges support from the Simons Foundation, Award 524259. This research of A.J.M. is partially supported by the Office of Naval Research ONR N00014-19-1-2286. D.Q. is supported as a postdoctoral fellow on the grant.

References

Abramov, R.V., Kovačič, G., Majda, A.J.: Hamiltonian structure and statistically relevant conserved quantities for the truncated Burgers-Hopf equation. Commun. Pure Appl. Math. **56**(1), 1–46 (2003)

Bajars, J., Frank, J.E., Leimkuhler, B.J.: Weakly coupled heat bath models for Gibbs-like invariant states in nonlinear wave equations. Nonlinearity **26**(7), 1945 (2013)

Benjamin, T.B., Feir, J.E.: The disintegration of wave trains on deep water part 1 theory. J. Fluid Mech. **27**(03), 417–430 (1967)

Blonigan, P.J., Farazmand, M., Sapsis, T.P.: Are extreme dissipation events predictable in turbulent fluid flows? Phys. Rev. Fluids **4**(4), 044606 (2019)

Bolles, C.T., Speer, K., Moore, M.N.J.: Anomalous wave statistics induced by abrupt depth change. Phys. Rev. Fluids **4**(1), 011801 (2019)

Camassa, R., McLaughlin, R.M., Moore, M.N.J., Yu, K.: Stratified flows with vertical layering of density: experimental and theoretical study of flow configurations and their stability. J. Fluid Mech. **690**, 571–606 (2012)

Chen, J., Pelinovsky, D.E.: Periodic travelling waves of the modified KdV equation and rogue waves on the periodic background. J. Nonlinear Sci. **29**(6), 2797–2843 (2019)

Chen, N., Majda, A.J.: Filtering nonlinear turbulent dynamical systems through conditional Gaussian statistics. Mon. Weather Rev. **144**(12), 4885–4917 (2016)

Clarkson, P.A., Dowie, E.: Rational solutions of the Boussines equation and applications to rogue waves. Trans. Math. Appl. **1**(1), tnx003 (2017)

Costa, A., Osborne, A.R., Resio, D.T., Alessio, S., Chrivì, E., Saggese, E., Bellomo, K., Long, C.E.: Soliton turbulence in shallow water ocean surface waves. Phys. Rev. Lett. **113**(10), 108501 (2014)

Cousins, W., Sapsis, T.P.: Unsteady evolution of localized unidirectional deep-water wave groups. Phys. Rev. E **91**(6), 063204 (2015)

Dematteis, G., Grafke, T., Onorato, M., Vanden-Eijnden, E.: Experimental evidence of hydrodynamic instantions: the universal route to rogue waves. Phys. Rev. X **9**(4), 041057 (2019)

Dematteis, G., Grafke, T., Vanden-Eijnden, E.: Rogue waves and large deviations in deep sea. Proc. Nat. Acad. Sci. **115**(5), 855–860 (2018)

Farazmand, M., Sapsis, T.P.: Reduced-order prediction of rogue waves in two-dimensional deep-water waves. J. Comput. Phys. **340**, 418–434 (2017)

Ganedi, L., Oza, A.U., Shelley, M., Ristroph, L.: Equilibrium shapes and their stability for liquid films in fast flows. Phys. Rev. Lett. **121**(9), 094501 (2018)

Garrett, C., Gemmrich, J.: Rogue waves. Phys. Today **62**(6), 62 (2009)

Gramstad, O., Zeng, H., Trulsen, K., Pedersen, G.K.: Freak waves in weakly nonlinear unidirectional wave trains over a sloping bottom in shallow water. Phys. Fluids **25**(12), 122103 (2013)

Guth, S., Sapsis, T.P.: Machine learning predictors of extreme events occurring in complex dynamical systems. Entropy **21**(10), 925 (2019)

Heller, E.J., Kaplan, L., Dahlen, A.: Refraction of a Gaussian seaway. J. Geophys. Res. Oceans **113**(C9) (2008)

Herterich, J.G., Dias, F.: Extreme long waves over a varying bathymetry. J. Fluid Mech. **878**, 481–501 (2019)

Holm, D.D.: A stochastic closure for wave-current interaction dynamics. J. Nonlinear Sci. **29**(6), 2987–3031 (2019)

Johnson, R.S.: A Modern Introduction to the Mathematical Theory of Water Waves, vol. 19. Cambridge University Press (1997)

Karmpadakis, I., Swan, C., Christou, M.: Laboratory investigation of crest height statistics in intermediate water depths. Proc. R. Soc. A **475**(2229), 20190183 (2019)

Kharif, C., Giovanangeli, J.-P., Touboul, J., Grare, L., Pelinovsky, E.: Influence of wind on extreme wave events: experimental and numerical approaches. J. Fluid Mech. **594**, 209–247 (2008)

Kleeman, R., Turkington, B.E.: A nonequilibrium statistical model of spectrally truncated Burgers-Hopf dynamics. Commun. Pure Appl. Math. **67**(12), 1905–1946 (2014)

Lax, P.D.: Periodic solutions of the KdV equation. Commun. Pure Appl. Math. **28**(1), 141–188 (1975)

Macêdo, A.M.S., González, I.R.R., Salazar, D.S.P., Vasconcelos, G.L.: Universality classes of fluctuation dynamics in hierarchical complex systems. Phys. Rev. E **95**(3), 032315 (2017)

Majda, A., Qi, D.: Strategies for reduced-order models for predicting the statistical responses and uncertainty quantification in complex turbulent dynamical systems. SIAM Rev. **60**(3), 491–549 (2018)

Majda, A.J.: *Introduction to Turbulent Dynamical Systems in Complex Systems*. Springer (2016)

Majda, A.J., Moore, M.N.J., Qi, D.: Statistical dynamical model to predict extreme events and anomalous features in shallow water waves with abrupt depth change. Proc. Natl. Acad. Sci. **116**(10), 3982–3987 (2019)

Majda, A.J., Qi, D.: Statistical phase transitions and extreme events in shallow water waves with an abrupt depth change. J. Stat. Phys. pp. 1–24 (2019)

McLachlan, R.: Symplectic integration of Hamiltonian wave equations. Numer. Math. **66**(1), 465–492 (1993)

Müller, P., Garrett, C., Osborne, A.: Rogue waves. Oceanography **18**(3), 66 (2005)

Onorato, M., Proment, D., El, G., Randoux, S., Suret, P.: On the origin of heavy-tail statistics in equations of the nonlinear Schrödinger type. Phys. Lett. A **380**(39), 3173–3177 (2016)

Onorato, M., Proment, D., Toffoli, A.: Triggering rogue waves in opposing currents. Phys. Rev. Lett. **107**(18), 184502 (2011)

Onorato, M., Suret, P.: Twenty years of progresses in oceanic rogue waves: the role played by weakly nonlinear models. Nat. Hazards **84**(2), 541–548 (2016)

Pelinovsky, E., Talipova, T., Kharif, C.: Nonlinear-dispersive mechanism of the freak wave formation in shallow water. Physica D **147**(1–2), 83–94 (2000)

Peregrine, D.H.: Water waves, nonlinear Schrödinger equations and their solutions. ANZIAM J. **25**(1), 16–43 (1983)

Qi, D., Majda, A.J.: Using machine learning to predict extreme events in complex systems. Proc. Natl. Acad. Sci. **117**(1), 52–59 (2020)

Randoux, S., Walczak, P., Onorato, M., Suret, P.: Intermittency in integrable turbulence. Phys. Rev. Lett. **113**(11), 113902 (2014)

Randoux, S., Walczak, P., Onorato, M., Suret, P.: Nonlinear random optical waves: Integrable turbulence, rogue waves and intermittency. Physica D **333**, 323–335 (2016)

Rey, V., Belzons, M., Guazzelli, E.: Propagation of surface gravity waves over a rectangular submerged bar. J. Fluid Mech. **235**, 453–479 (1992)

Ristroph, L., Moore, M.N.J., Childress, S., Shelley, M.J., Zhang, J.: Sculpting of an erodible body in flowing water. Proc. Natl. Acad. Sci. **109**(48), 19606–19609 (2012)

Sapsis, T.P., Majda, A.J.: Blending modified Gaussian closure and non-Gaussian reduced subspace methods for turbulent dynamical systems. J. Nonlinear Sci. **23**(6), 1039–1071 (2013a)

Sapsis, T.P., Majda, A.J.: Statistically accurate low-order models for uncertainty quantification in turbulent dynamical systems. Proc. Nat. Acad. Sci. **110**(34), 13705–13710 (2013b)

Sapsis, T.P., Majda, A.J.: A statistically accurate modified quasilinear Gaussian closure for uncertainty quantification in turbulent dynamical systems. Physica D **252**, 34–45 (2013c)

Toffoli, A., Proment, D., Salman, H., Monbaliu, J., Frascoli, F., Dafilis, M., Stramignoni, E., Forza, R., Manfrin, M., Onorato, M.: Wind generated rogue waves in an annular wave flume. Phys. Rev. Lett. **118**(14), 144503 (2017)

Trulsen, K., Raustøl, A., Jorde, S., Rye, L.: Extreme wave statistics of long-crested irregular waves over a shoal. J. Fluid Mech. 882 (2020)

Viotti, C., Dias, F.: Extreme waves induced by strong depth transitions: Fully nonlinear results. Phys. Fluids **26**(5), 051705 (2014)

Viotti, C., Dutykh, D., Dudley, J.M., Dias, F.: Emergence of coherent wave groups in deep-water random sea. Phys. Rev. E **87**(6), 063001 (2013)

White, B.S., Fornberg, B.: On the chance of freak waves at sea. J. Fluid Mech. **355**, 113–138 (1998)

Whitham, G.B.: Linear and nonlinear waves, vol. 42. John Wiley & Sons (2011)

Ying, L.H., Zhuang, Z., Heller, E.J., Kaplan, L.: Linear and nonlinear rogue wave statistics in the presence of random currents. Nonlinearity **24**(11), R67 (2011)

Zakharov, V.E.: Turbulence in integrable systems. Stud. Appl. Math. **122**(3), 219–234 (2009)